Time-dependent near-blackbody thermal emission from pulsed laser irradiated vertically aligned carbon nanotube arrays

Raúl Fainchtein,[1,*] David M. Brown,[1] Karen M. Siegrist,[1] Andrew H. Monica,[1] Ehren Hwang,[2] Stuart D. Milner,[3] and Christopher C. Davis[2]

[1]*The Johns Hopkins University Applied Physics Laboratory, Laurel, Maryland, USA*
[2]*Department of Electrical and Computer Engineering, the University of Maryland, College Park, Maryland, USA*
[3]*Department of Civil and Environmental Engineering, the University of Maryland, College Park, Maryland, USA*

(Received 8 December 2011; published 26 March 2012)

Vertically aligned carbon nanotube (VACNT) arrays have been reported to be the "blackest" material fabricated to date. They also have a thermal conductivity parallel to the VACNT axis that is much larger than their thermal conductivity perpendicular to the axis. Even so, because of their large length-to-radius ratio, they can be assumed to have the same temperature in any cross section that is perpendicular to the tube axis. Consequently, a pulsed-laser irradiated VACNT array is a candidate to produce fast thermal emissions from the face of a VACNT array grown on a high thermal conductivity substrate. This can be represented as a one-dimensional thermal conductivity problem, where the proximal end of the carbon nanotubes (CNTs) jumps in temperature when irradiated with a pulsed laser, and the tubes then cool by thermal conduction down their axis to their distal end on a substrate where the temperature is fixed. We have measured and calculated analytically the time-dependent infrared (IR) emission from a range of VACNT arrays with different tube lengths grown on aluminum-nitride (AlN) and silicon-dioxide–silicon (SiO_2/Si) substrates. In a parallel effort to characterize their "blackness," we measured the spectral reflectance and emissivity and single-wavelength bidirectional reflectance distribution functions (BRDFs) of these arrays and found these optical characteristics compare well to ideal blackbody behavior. Shorter CNTs exhibit faster cooling than longer nanotubes, and the effective axial conductivity has been determined by comparison between experimental IR signatures and theoretical modeling of expected temperature distributions. Our key finding is that VACNT arrays can act as very fast on-off blackbody sources, which can be useful in many applications requiring such a source.

DOI: 10.1103/PhysRevB.85.125432 PACS number(s): 78.20.nd, 78.67.Ch, 65.80.−g

I. INTRODUCTION

We have been studying the emission and reflection characteristics of pulsed-laser irradiated vertically aligned carbon nanotube (VACNT) arrays, which were initially shown to have the highest absorptivity of any known material by Yang *et al.*[1] Subsequent research has confirmed the almost perfect "blackness" of VACNTs of single- and multi-walled VACNTs.[2–8] The normal spectral emissivity of single-walled VACNTs has been shown to be >0.98 over a wavelength range from 5 to 12 μm and their reflectance to be <0.02 over a wavelength range from 0.2 to 200 μm.[6] Some bidirectional reflectance distribution functions (BRDFs) at a single wavelength of 633 nm have been reported.[3,7] A low-density multi-walled VACNT layer on an arbitrarily-shaped surface has been shown to be a near perfect absorber and impedance-matching layer.[5] Yang *et al.*[8] have reported the lowest measured reflectance from a VACNT sample of 0.0003 over a wavelength range from 3 to 13 μm, and confirmed the near-perfect blackbody spectral emissivity of samples heated in the range 450–600 K. Theoretical analyses have helped to elucidate the role of CNT length, intertube spacing, and polarization of radiation incident on the end face of the VACNT array, and they have shown that absorbance increases with tube length, with infinitely long tubes being perfect absorbers.[2] Thus work has also shown that the reflectance of VACNTs shows some variation with wavelength for tubes a few μm long. The extremely weak scattering of light from the surface of VACNTs can be attributed in a simple sense to the fact that CNTs have a low volume fraction compared to the air spaces in between tubes, so that the effective refractive index of the array is close to unity.[8]

There have been no previous reports of the temporal signatures of the emission from VACNTs irradiated with a pulsed laser, where there is a rapid jump in the temperature of the proximal face of the VACNT array. It is the study of these temporal signatures, and how they are affected by tube length and array spectral properties, that is the primary focus of this paper. CNTs have been shown to conduct heat extremely efficiently along their axes,[9] so they rapidly transfer heat to a thermally conductive substrate and cool rapidly after laser irradiation of a specific region terminates. In our experiments, the arrays were irradiated with a pulsed laser focused to a Gaussian spot on the end faces of the array, as shown in Fig. 1. The time dependence of the emission from the CNTs was measured with a fast mercury cadmium telluride (HgCdTe) detector, and the pattern of illumination on the end faces of the array was imaged with a liquid nitrogen (LN_2) cooled focal plane array (FPA) indium antimonide (InSb) camera with a germanium objective lens. CNTs have a large aspect ratio with radial dimensions in the nanometer range and axial dimensions in the range of many micrometers to more than 1 millimeter. If a macroscopic VACNT array is irradiated with a short pulse laser, the surface of the array is heated almost instantaneously. The absorption of laser energy in the proximal ends of the CNTs produces an extremely fast jump in temperature of a thin layer at the end face. Emission from the end face of the array is a function of the end-face temperature. As this heat is conducted rapidly away down the axis of the tubes, the end

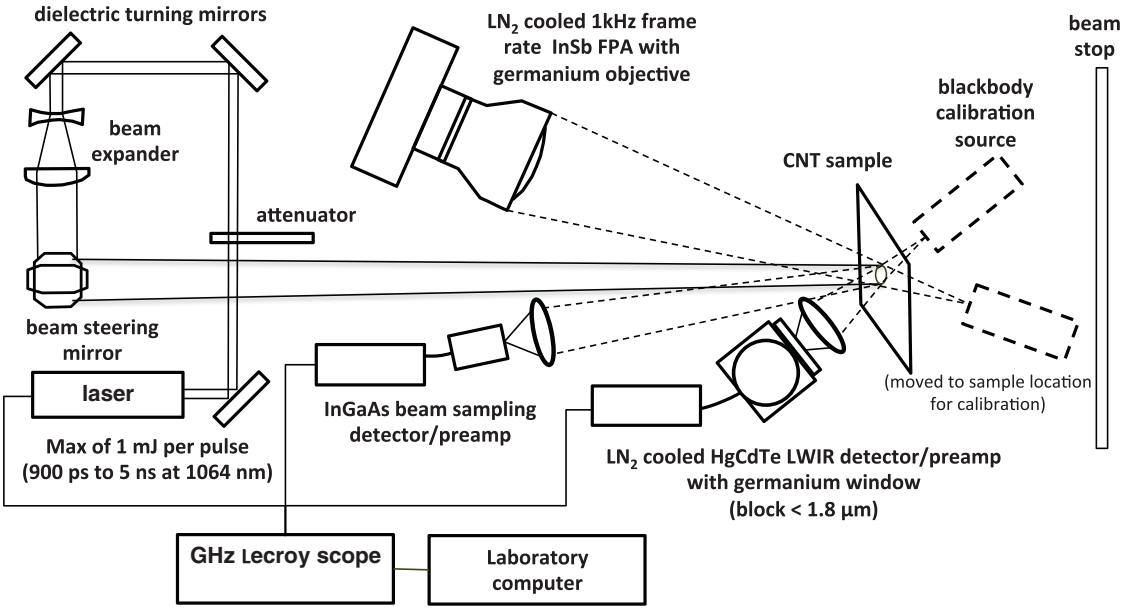

FIG. 1. Experimental arrangement for pulsed laser irradiation of VACNT arrays and calibration of their emission against a blackbody source.

faces cool rapidly after laser irradiation ceases, thus leading to a fast decay of the emission.

To further characterize the optical properties of the VACNTs we measured the spectral reflectance and emissivity and single-wavelength BRDFs of these arrays.

II. TIME-RESOLVED EMISSION SIGNATURES OF PULSED-LASER IRRADIATED VACNTS

The CNT samples were illuminated with a 1.06 μm Nd:YAG pulsed-laser system (Continuum Minilite II). The system nominally operates at 15 Hz with a pulse length of 5–7 ns, and a maximum pulse energy of 50 mJ. At maximum energy, the CNT samples are easily burned; hence, the laser is operated in low-energy mode and attenuated typically to 1 mJ per pulse. The full system setup is shown in Fig. 1. After the appropriate attenuation, the laser is steered through a series of mirrors and projected onto the VACNT sample. The beam is roughly 3 mm in diameter when it strikes the VACNT sample, which is nearly the same size as a blackbody calibration source that we used. The interaction of the laser radiation with the VACNT sample is monitored by three detectors. The first of these detectors is an indium gallium arsenide (InGaAs) avalanche photodiode with a 1-GHz bandwidth (Menlo Systems, Model APD310), which is used to monitor the laser pulse shape (temporal) and timing jitter. The second detector is a 100-MHz HgCdTe detector with matched preamplifier (Teledyne Judson Technologies, Model J15D14-M204-S02M-60) used to monitor the thermal IR response of the CNT sample. A germanium window (negligible transmission below 1.8 μm) in front of the HgCdTe detector ensures that the detector responds to the thermal IR signature only and not the incident pump laser source. Additionally, a 1-inch-diameter zinc selenide (ZnSe) lens with a 1-inch focal length is used to collect the thermal radiation emitted from the sample. The responses of the InGaAs and HgCdTe detectors are triggered using the Q switch of the laser and digitized using a 3-GHz oscilloscope (Lecroy WavePro 7300A). The third characterization tool is a high frame rate (1-kHz) InSb camera (Amber Galileo, FPA: AE173-1, 256 × 256), operated with a 0.23-ms integration time and a neutral density filter with an optical density of 2 inserted in its optical path. The thermal IR camera and HgCdTe single-element detector are calibrated using a blackbody calibration source (Electro Optical Industries, Inc., Model 19708S1/LS). In both cases, the aperture of the blackbody is positioned at the location of the VACNT sample to reduce error caused by dissimilar ranges between the calibration and measurement. As the blackbody temperature is slowly increased, multiple measurements are taken with the camera and the single-element detector to remove the effects of detector nonlinearity.

III. GROWTH TECHNIQUES

CNT arrays are grown on AlN or SiO_2/Si substrates.[10,11] The AlN substrates use wafers diced into 25-mm^2 pieces. Using an *e*-beam evaporation system, iron is deposited at a rate of 0.1 nm per second for a final film thickness of 2 nm. The substrates are then cleaned by rinsing sequentially with trichloroethylene, toluene, acetone, and finally isopropyl alcohol. The substrates are then dried with nitrogen. The VACNT growths were performed in a 50-mm-diameter quartz tube furnace (Thermolyne Model 79345) heated to 750 °C. Prior to sample insertion into the furnace tube, wet and dry argon were flowed at rates of 10 and 500 sccm, respectively, for 10 minutes, after which time hydrogen was introduced at a rate of 250 sccm and allowed to flow for another 10 minutes. At this time, the sample was placed onto a quartz rod and inserted into the furnace at a rate of 25 mm/s, reaching the central heating zone of the furnace in approximately 10 seconds. The sample remains in this environment for 5 minutes prior to carbon seed gas exposure. The seed gas, ethylene (C_2H_4), was

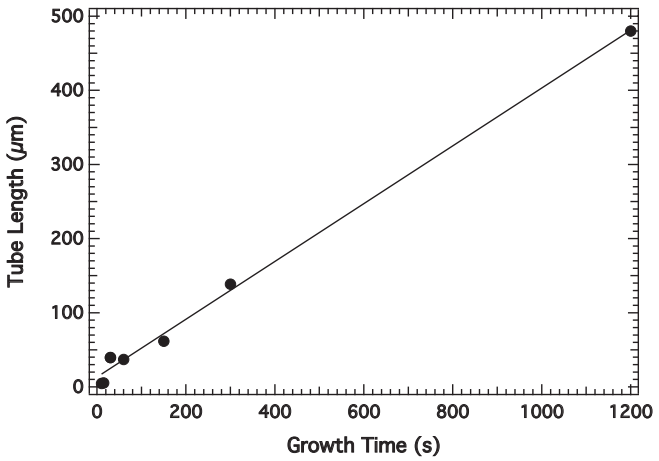

FIG. 2. VACNT length vs. growth time measured by SEM (line is a least-squares linear fit).

then flowed at a rate of 300 sccm for the prescribed growth time, typically ranging from 5 seconds to 15 minutes. After the growth time elapsed, the C_2H_4 was shut off and the sample was allowed to dwell for 10 minutes in the furnace. The sample was then removed from the tube furnace and allowed to cool to room temperature. Grown CNT arrays were characterized by scanning electron microscopy (SEM) to determine their morphology and lengths. Our tubes are multi-wall CNTs. The variation of CNT length versus growth time is shown in Fig. 2.

Figure 3 shows some example SEM images. A few general comments can be made regarding the morphology of arrays of different length tubes: (1) the longer the growth time, the more the CNTs form a vertically aligned mat; (2) arrays grown for a short time are less ordered in the vertical direction; (3) individual tubes are never exactly straight and meander in the radial direction; and (4) the diameter of individual tubes varies from 6 to 20 nm. The length of tubes is determined by examining the sides of grown arrays, which are usually less ordered than tubes in the center of the mat.

IV. CALIBRATION OF TEMPERATURE FOR INFRARED EMISSIONS

Images of the illuminated region on the proximal face are used to determine the Gaussian spot size of the illuminating laser beam, as shown in Fig. 4.

The total power from the Gaussian spot is focused onto the HgCdTe detector, and the signal level is compared with the signal produced by a blackbody source whose emitting aperture is also focused on the HgCdTe detector. The power emitted by the blackbody source and collected by the IR detector is

$$P_{BB} = A\varepsilon\Delta\omega\sigma T^4. \quad (1)$$

The blackbody overfills the collection field of view (FOV); hence, A is the collection area of the detector optics; ε is the emissivity, which is assumed to be one; $\Delta\omega$ is an effective collection solid angle; and σ is the Stefan-Boltzmann constant. The VACNTs are illuminated with a Gaussian beam for which the intensity profile is

$$I(r) = I_0 e^{-2r^2/w^2}, \quad (2)$$

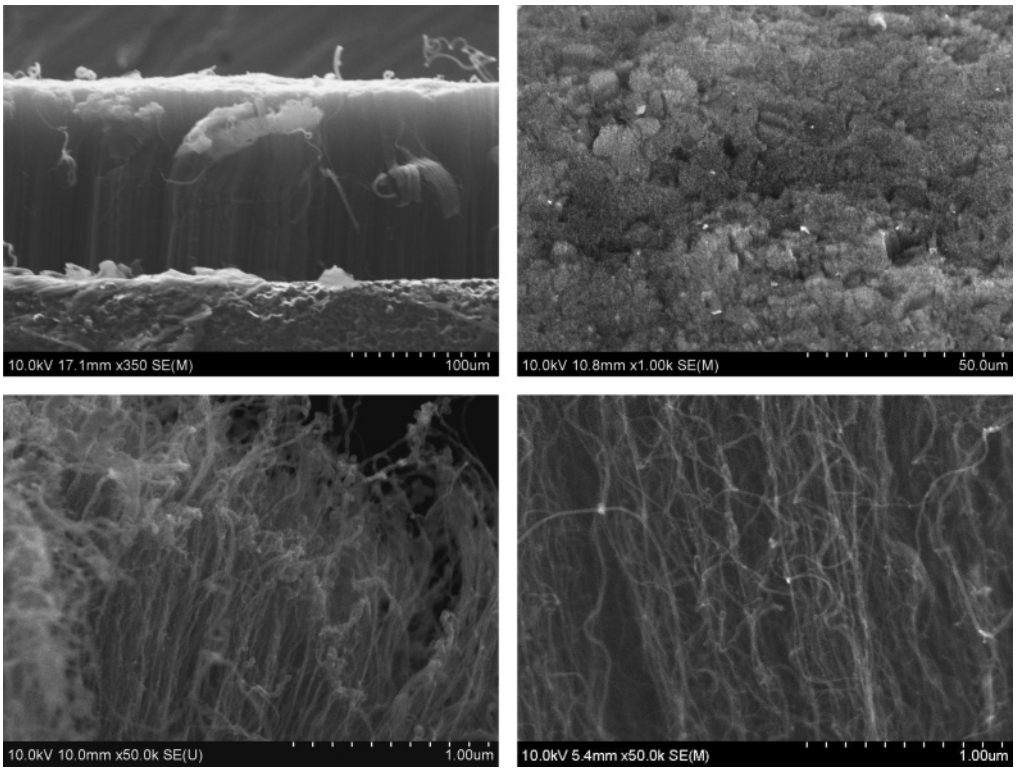

FIG. 3. VACNT arrays grown on AlN, from top left clockwise: side view, top view, view close to the tube ends, and higher magnification side view.

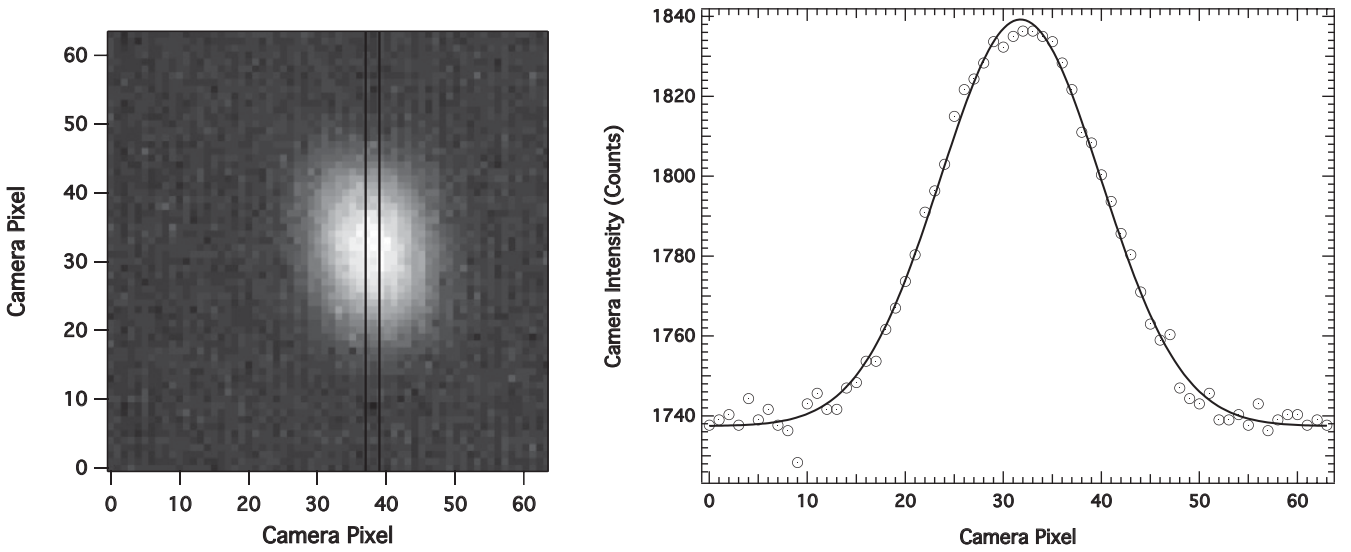

FIG. 4. On the left, image of illuminated region of VACNT array face. On the right, 2–pixel-wide averaged line scans of the marked left image region and corresponding Gaussian fit (solid line).

where w is the spot size (i.e., the $1/e$ radius of the field distribution of the beam). The initial radial temperature distribution of the irradiated VACNTs is

$$T_i(r) = T_0 e^{-2r^2/w^2} + T_a, \tag{3}$$

where T_a is ambient temperature. The temperature of the surface of the VACNTs as a function of time is

$$T(r,t) = T_0 e^{-2r^2/w^2} f(t) + T_a. \tag{4}$$

The power collected from an irradiated VACNT sample is

$$P_{\mathrm{CNT}}(t) = 2\pi\sigma\,\Delta\omega_{\mathrm{CNT}}\varepsilon_{\mathrm{CNT}} \int_0^a [T(t,r)]^4\, dr$$
$$= 2\pi\sigma\,\Delta\omega_{\mathrm{CNT}}\varepsilon_{\mathrm{CNT}} \int_0^a \left(T_0 e^{-2r^2/w^2} + T_a\right)^4 dr, \tag{5}$$

where a is the radius of the overfilled FOV of the collection optics, $\Delta\omega_{\mathrm{CNT}}$ is the effective collection solid angle for the CNTs, and $\varepsilon_{\mathrm{CNT}}$ is the emissivity of the CNTs, which is assumed to be wavelength independent and equal to 1. The initial power from the center of the irradiated CNTs at $t = 0$ is

$$P_{\mathrm{CNT}}(t) = 2\pi\sigma\,\Delta\omega_{\mathrm{CNT}}\varepsilon_{\mathrm{CNT}} \int_0^a [T_0 + T_a]^4\, dr. \tag{6}$$

Comparisons of the signals from blackbody and VACNT allowed a calibration curve that provided peak VACNT temperatures as a function of detector signal. Figure 5 shows some typical temperature-time signatures from VACNT arrays of different lengths grown on AlN. This work focuses on the radiometric behavior of VACNTs on AlN because the high thermal conductivity, between 140 and 180 W $\mathrm{m}^{-1}\mathrm{K}^{-1}$, of the AlN substrate provided faster decay thermal signatures. These thermal signatures are observed from the proximal face of the VACNT arrays, as has been described previously by Cho and Davis,[12] rather than the standard "laser flash" method used to measure the thermal diffusivity of CNTs by Akoshima *et al.*[13] The experimental curves in Fig. 5 have not been normalized. Different VACNT samples show some variability in the amplitude of observed signals because of likely differences in sample morphology and small variations of collection geometry, since not all these curves were collected at the same time.

These temperature-time curves can be analyzed to determine the thermal characteristic of the CNTs in the array, as will be shown later.

To support our studies of the time-resolved emission characteristics of VACNT we also performed some spectral reflectance, BRDF, and emissivity experiments. Similar measurements have been made on VACNT arrays by others, but we felt it was important to confirm that our samples were truly "black" and had optical properties in the CW domain that were similar to previous reports. Our observational wavelength regions are also not the same as in previous reports so they extend our knowledge of these characteristics. The details of these experiments and the results are given in the Appendices.

V. THEORETICAL ANALYSIS OF THERMAL EMISSION CHARACTERISTICS OF VACNT ARRAYS

The geometry of an idealized single CNT being analyzed is shown in Fig. 6.

If one assumes that absorption only occurs through the end face of each CNT, the initial temperature elevation is determined by the irradiation laser fluence and decays exponentially down the axis of the nanotube. For example, with initial laser intensity I_0, for an absorptivity α, the intensity at distance z along the axis from the front face at $z = 0$ is

$$I(z) = I_0 e^{-\alpha z}. \tag{7}$$

The irradiating laser pulse is assumed to be short enough so that no significant heat conduction occurs during the laser pulse. The characteristic thermal conduction time in cylindrical geometry can be written as

$$\tau_c = \frac{a^2}{4\kappa}, \tag{8}$$

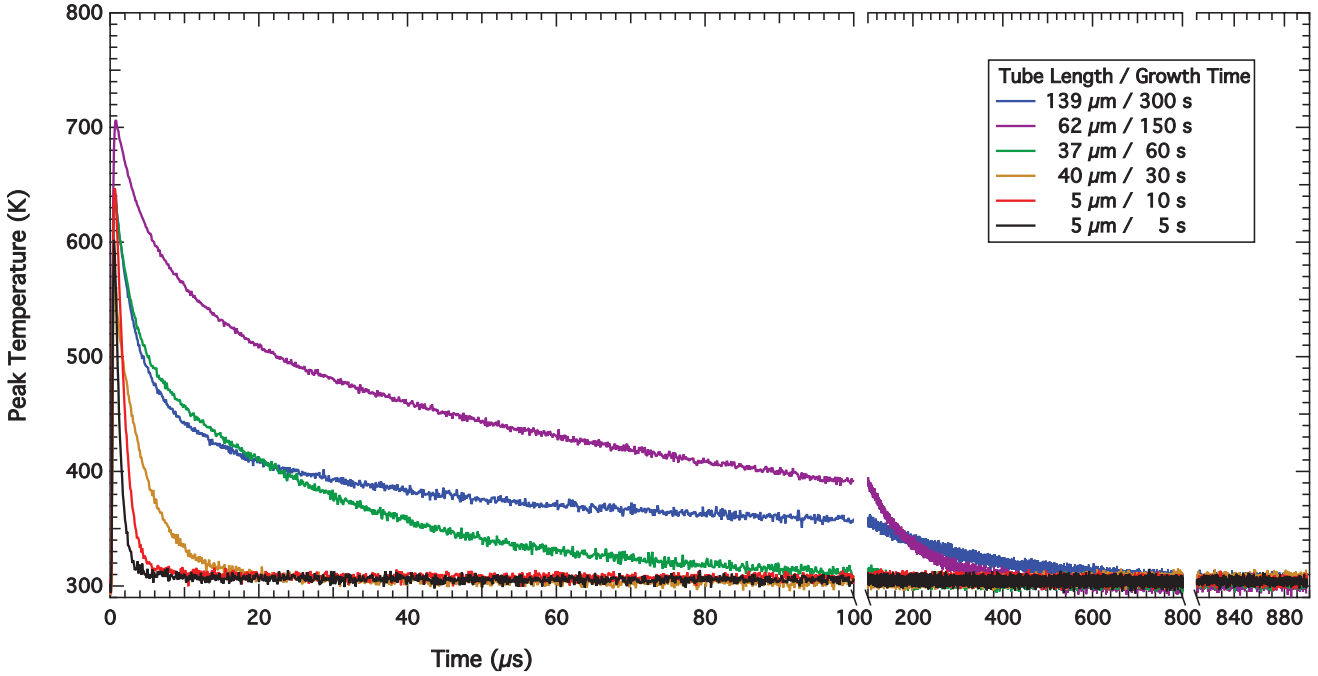

FIG. 5. (Color) Temperature-time signatures from VACNT arrays of various lengths grown on AlN.

where a is the radius and κ is the thermal diffusivity defined by

$$\kappa = \frac{k}{\rho C_p}, \tag{9}$$

with k being the thermal conductivity, ρ the density, and C_p the specific heat. For CNTs, not all the quantities in Eqs. (7)–(9) are well known, and likely depend on exact CNT morphology. However, some general observations can be made.

The thermal conductivity of CNTs is much larger in the axial compared to the radial direction. Along the tube axis the thermal conductivity is very high and may approach 3000 W m^{-1}K^{-1} at room temperature,[13] although values given in the literature vary and clearly depend on the length and arrangement of CNTs used in the measurements (see Ref. 13 and references therein). For example, Yi *et al.*[14] report a value of about 25 W m^{-1}K^{-1} for 1-mm-long CNTs, which varies approximately linearly with temperature. The thermal conductivity perpendicular to the tube axis is much smaller, on the order of 1.5 W m^{-1}K^{-1}, comparable to the conductivity of soil. The density of CNTs is on the order of 1300 kg m^{-3}. The specific heat of CNTs is also approximately linear with temperature,[4] having a value at 300 K of about 450 J kg^{-1}K^{-1}. Measurements show that single-walled carbon nanotubes have a room-temperature thermal conductivity along their axis of about 3500 W m^{-1}K^{-1}. These numbers allow some estimates of thermal conduction times to be made. For example, for a 10-nm-diameter CNT at 300 K using a reported value of 25 W m^{-1}K^{-1}, the axial thermal conductivity can be written as $k_{\text{axial}}(T) = 25\frac{T}{300}$ and the radial thermal conductivity as $k_{\text{radial}}(T) = 1.5\frac{T}{300}$. In this case the axial thermal diffusivity is 4.2 $\times$ 10^{-5} m^2 s^{-1}. In some of the simulations that follow we have used a value of k = 750 W m^{-1}K^{-1} when the axial thermal diffusivity is 1.25 $\times$ 10^{-3} m^2 s^{-1}. Because the specific heat likely varies approximately linearly with temperature, the thermal diffusivity likely remains more or less constant with temperature, which has been verified up to a temperature of 500 °C by Xie *et al.*[15] The characteristic thermal conduction time in the radial direction for a 10-nm nanotube is about 2.5 ps. For a 100-μm-long CNT in the axial direction, the thermal conduction time is on the order of 60 μs for a thermal diffusivity of 2 $\times$ 10^{-6} m^2 s^{-1} or about 8 μs for a thermal diffusivity of 1.25 $\times$ 10^{-3} m^2 s^{-1}, although these times will be much shorter depending on the tube morphology: single- or multi-walled, and length. Based on these numbers, it is reasonable to assume that an irradiated CNT reaches a temperature that is constant in the radial direction but varies in the axial direction.

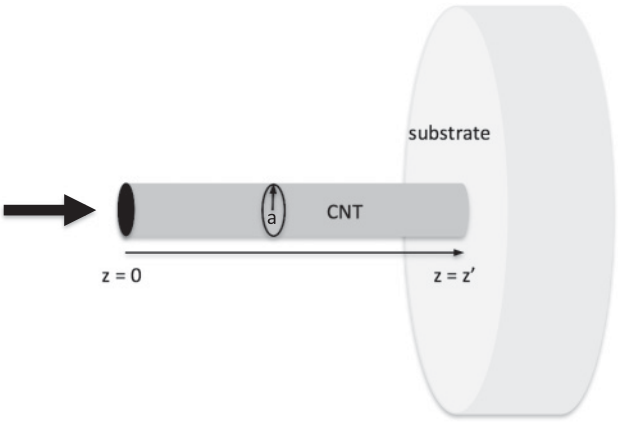

FIG. 6. CNT irradiation geometry.

Because of the small distance between adjacent tubes in the VACNT array, which is much smaller than the wavelength of the illuminating laser, and the relatively high electrical conductivity of the CNTs, incident radiation will not penetrate very far beyond the proximal face of the CNTs. If the CNTs

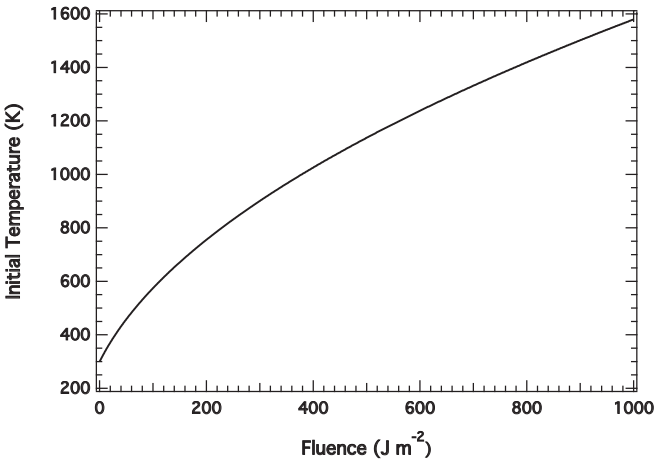

FIG. 7. Temperature at end face of CNT for end-face absorption only, calculated assuming an absorption depth of 0.42 μm.

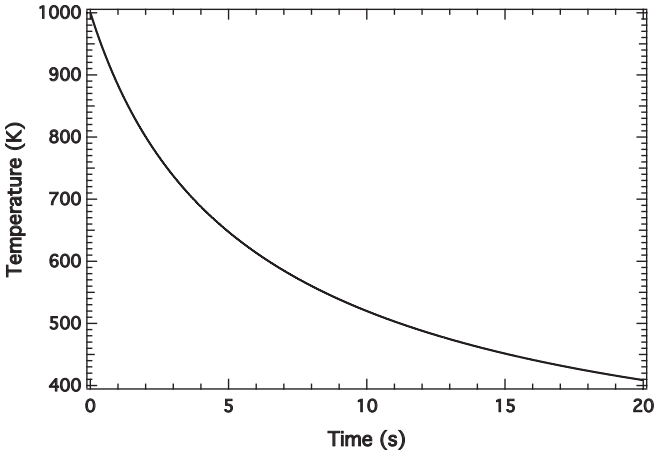

FIG. 8. Radiative cooling of 100-μm-long CNT assuming initial temperature of 1000 K and ambient temperature of 300 K.

only absorb through their end faces, the radiation is absorbed within a skin depth δ on the order of 0.4 μm, a distance over which the thermal conduction time is about 1 ns. Previously published work indicates that radiation can penetrate several μm into a VACNT array because of the low volume-filling fraction of the tubes themselves,[2,4] but it is not clear how much this radiation in the air gaps between tubes extends the initially heated region of the tubes.

If the length over which the proximal ends of the tubes is heated is δ, then the effective volume of each CNT being heated is initially only $\pi a^2\delta$, and the temperature reached at the face of the CNT is

$$T_i = \sqrt{\frac{4\pi a^2 F}{3\rho V_{\mathrm{CNT}}} + T_a^2}, \tag{10}$$

where $V_{\mathrm{CNT}} = \pi a^2\delta$, so the initial temperature is

$$T_i = \sqrt{\frac{4F}{3\rho\delta} + T_a^2}. \tag{11}$$

Figure 7 shows the temperature increase as a function of incident fluence.

VI. THERMAL EXPANSION

If a CNT is elevated in temperature by 1000 K in 7 ns, the increase in length of a 100-μm-long CNT is on the order of 70 nm, and velocity of expansion is 10 m s^{-1}, which is not supersonic. If a sound is heard when the energy is absorbed, this is caused by this expansion, but not because the expansion is supersonic. This is a classic photoacoustic phenomenon.[16] The air adjacent to the CNT is adiabatically compressed by the CNT motion. The velocity of sound in CNTs is believed to be at least comparable to diamond, 12000 m s^{-1}, so the acoustic transit time along a 100-μm-long tube is about 8 ns.

VII. RADIATIVE COOLING

If an array of CNTs is heated, radiative cooling through the end face must be taken into account. On the other hand, cooling through the walls will not be effective because of the thermal balance between heat radiated from one CNT and heat absorbed from nearby radiating CNTs at the same temperature. If we assume that a CNT after heating is at a uniform temperature T, the thermal energy stored in the CNT is

$$U = AL\rho C_p(T)T, \tag{12}$$

where A is the area of the end face and L is the length of the radiative region. The radiative loss of energy from the CNT through its end face is

$$\frac{dU}{dt} = A\sigma\left(T^4 - T_a^4\right), \tag{13}$$

where σ is the Stefan-Boltzmann constant. Combining Eqs. (12) and (13) gives

$$\sigma\left(T^4 - T_a^4\right) = -\frac{d}{dt}[L\rho C_p(T)T] = -L\rho\frac{d}{dt}[C_p(T)T]. \tag{14}$$

If C_p is assumed to vary as $C_p(T) \approx 1.5T$, this gives

$$\frac{dT}{dt} = -\frac{\sigma\left(T^4 - T_a^4\right)}{3L\rho T}. \tag{15}$$

Figure 8 shows the numerically calculated solution to this equation for a 100-μm-long CNT, an initial temperature of 1000 K, and an ambient temperature of 300 K. It is clear that the radiative cooling through the end face of the CNT is much slower than the thermal conduction cooling time.

VIII. TIME-DEPENDENT TEMPERATURE IN A CNT WITH VARIOUS BOUNDARY CONDITIONS

The time dependence of the temperature distribution in a VACNT can be calculated using appropriate Green's functions. The full differential equation to be solved is

$$\frac{\partial^2 T}{\partial r^2} + \frac{1}{r}\frac{\partial T}{\partial r} + \frac{1}{r^2}\frac{\partial^2 T}{\partial \phi^2} + \frac{\partial^2 T}{\partial z^2} + \frac{g(r,\phi,z,t)}{k} = \frac{1}{\kappa}\frac{\partial T}{\partial t}, \tag{16}$$

where k is the thermal conductivity, κ is the thermal diffusivity, and $g(r,\phi,z,t)$ is the heat generation rate as a function of position

and time. With the radial and azimuthal symmetry of a VACNT, this equation reduces to

$$\frac{\partial^2 T}{\partial z^2} + \frac{g(r,\phi,z,t)}{k} = \frac{1}{\kappa}\frac{\partial T}{\partial t}. \quad (17)$$

The Green's function solution to this problem amounts to solving the temperature *T(z,t)* that results from a delta-function heat input of the form $g(z,t) = \delta(z - z')\delta(t - \tau)$. In a cylinder this corresponds to delta-function heat input in an infinitesimal slab at $z = z'$ at time $t = \tau$. The appropriate Green's function also includes the boundary conditions. Two boundary conditions have been considered. These models assume that the thermal diffusivity is constant over the range of temperatures studied, which has been confirmed previously by Xie *et al.*[15] at least up to 500 K.

IX. DISTAL END OF CNT HELD AT ZERO TEMPERATURE WITH NO HEAT FLOW AT PROXIMAL FACE

In this case, the boundary conditions imposed are holding the distal end of the VACNT at a fixed zero temperature, and no heat conduction at the proximal end of the tube where the irradiation occurs. In reality this is only an approximation because some radiation will occur, but this will be negligible compared to the thermal conduction along the tube axis. The Green's function for this problem has been given by Carslaw and Jaeger[17] and by Beck *et al.*[18] In the notation used by Beck *et al.*, it can be written as

$$G_{21z}(z,y|z',\tau) = \frac{2}{L}\sum_{m=1}^{\infty} e^{-\beta_m^2 \kappa(t-\tau)/L^2} \cos\left(\beta_m \frac{z}{L}\right) \cos\left(\beta_m \frac{z'}{L}\right), \quad (18)$$

where $\beta_m = \pi(m - 1/2)$ and L is the length of the CNT.

For small values of t, such that $\kappa(t - \tau)/L^2 \leqslant 0.022$, a better version of this function to use is

$$G_{21z}(z,y|z',\tau) = [4\pi\kappa(t-\tau)]^{-1/2}\left\{\exp\left[-\frac{(z-z')^2}{4\kappa(t-\tau)}\right] + \exp\left[-\frac{(z+z')^2}{4\kappa(t-\tau)}\right] - \exp\left[-\frac{(2L-z-z')^2}{4\kappa(t-\tau)}\right]\right\}. \quad (19)$$

Figure 9 shows the temperature dependence at $z = 0$ for an impulse excitation at $z = 0$. Note that as $t \to 0$, $T \to \infty$ because this is the graph of a delta-function impulse at $t = 0$. These analytical solutions to the temperature have been checked against finite element solutions from COMSOL Multiphysics software with perfect agreement.

In reality, CNTs do not have perfect absorptivity and, indeed, their precise absorption coefficients likely vary with morphology. Haque *et al.*[19] provides an absorption coefficient of 2.4×10^6 m^{-1}, which is used here. If all radiation is assumed to be absorbed traveling parallel to the tube axis, the temperature distribution that results can be calculated from

$$T_{\text{axial}}(z,t) \propto \int_0^L G(z,t|z',\tau) e^{-\alpha z'} dz. \quad (20)$$

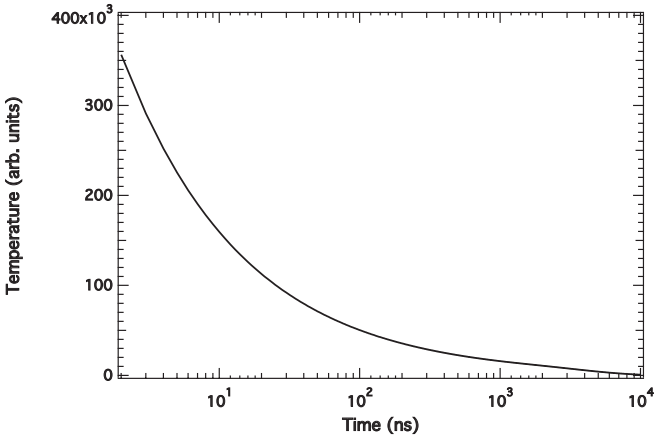

FIG. 9. Time dependence at the irradiated endface ($z = 0$) for a delta function energy input at $z = 0$ and a 100-μm-long CNT calculated from Eqs. (20) and (21) using a thermal diffusivity of 1.253×10^{-3} m^2 s^{-1}. The longer decay time constant is 3.2 μs.

X. TEMPERATURE DEPENDENCE WITH DIFFERENT BOUNDARY CONDITIONS

Analytic solutions to the temperature of a CNT can also be given for two other interesting boundary conditions: (1) no heat flow to the substrate at the distal end of the CNT and (2) with contact resistance at the substrate where the Green's function for heat flow obeys the following:

$$k\frac{\partial G}{\partial z} + h_2 G = 0, \quad (21)$$

where k is the thermal conductivity and h_2 is a heat transfer coefficient (W m^{-2}K^{-1}).

In the case of no heat flow to the substrate, the temperature at the proximal end of the CNT is[17]

$$G_{21z}(z,y|z',\tau) = \frac{1}{L}\left[1 + 2\sum_{m=1}^{\infty} e^{-\beta_m^2\kappa(t-\tau)/L^2} \cos\left(\beta_m \frac{z}{L}\right) \times \cos\left(\beta_m \frac{z'}{L}\right)\right], \quad (22)$$

where $\beta_m = m\pi$. This Green's function is the temperature distribution at z at time t for an instantaneous sheet heat source at z' at time τ.

In the case of contact resistance at $z = L$, the appropriate Green's function is[18]

$$G_{21z}(z,y|z',\tau) = \frac{1}{L}\left[1 + 2\sum_{m=1}^{\infty} e^{-\beta_m^2\kappa(t-\tau)/L^2} \cos\left(\beta_m \frac{z}{L}\right) \times \cos\left(\beta_m \frac{z'}{L}\right)\right], \quad (23)$$

where $B = \frac{h_2 L}{k}$. For $m \geqslant 1$, and large B

$$\beta_m = \frac{(2m-1)\pi B}{2(B+1)} \times \left\{1 + \frac{[(2m-1)\pi]^2}{12(B+1)^3 + [(2m-1)\pi]^2(2B-1)}\right\}, \quad (24)$$

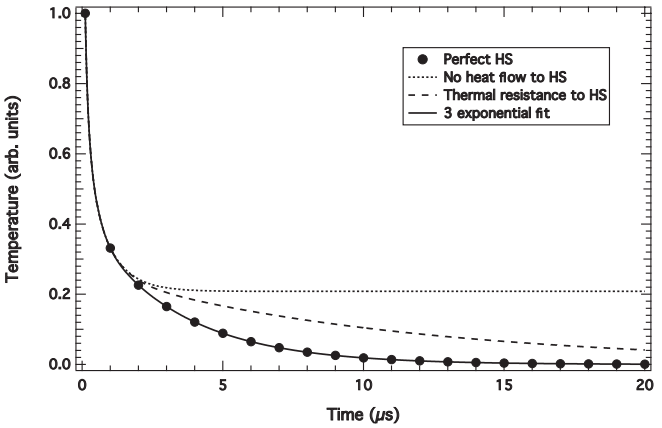

FIG. 10. Temperature dependence of end face of 100-μm CNT; using a thermal diffusivity of 1.253×10^{-3} m^2 s^{-1} for different boundary conditions at the heat sink. Calculated using Eqs. (23)–(26)

and for $0 \leqslant B \leqslant 2$

$$\beta_1 = \left\{ \frac{2B}{3+B}\left[1 - \frac{1}{45}\left(\frac{3B}{3+B}\right)^2\right]\right\}^{1/2} \frac{\delta y}{\delta x}. \tag{25}$$

For $m \geqslant 2$ and small B

$$\beta_m = \frac{(m-1)\pi}{2(B+3)}\left\{2B + 3 + 3\left[1 + \frac{4B(B+2)}{3(m-1)^2\pi^2}\right]^{1/2}\right\}. \tag{26}$$

Figure 10 gives an example of the results obtained with such calculations.

These simulations show that the temperature of the proximal ends of the CNTs decays faster for shorter tubes and also faster for larger thermal diffusivity values. If the CNTs are isolated from the substrate, they reach a final equilibrium temperature determined by the total amount of absorbed energy and the tube length. The temperature versus time behavior with a perfect substrate heat sink fits a three-exponential function extremely well. The variation of these three time constants for 100-μm CNTs for different values of the diffusivity is shown in Fig. 11. The shortest of the three time constants predicted theoretically are shorter than the time resolution of the infrared detector that we used.

It should be pointed out that these are least-squares fits of calculated time-dependent thermal signatures. There is no fundamental theoretical justification for these signatures to be multiexponential, but analysis of observed signatures in this way allows a comparison with theoretical time signatures. It is perhaps reasonable to explain the multiexponential behavior qualitatively in the following way: (a) the incident radiation is absorbed in a short proximal region of the tube near the irradiated face, and this short region conducts heat very rapidly into adjacent unheated regions of the tube; (b) the whole tube becomes heated, contributing a second time constant; and (c) the tubes dump their heat into the substrate, giving a third time constant.

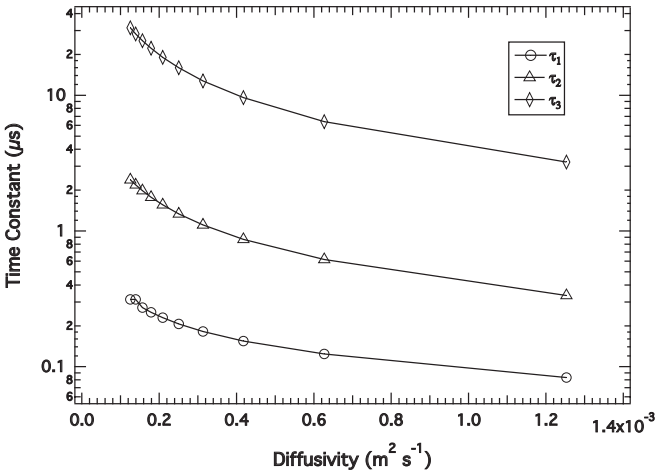

FIG. 11. Calculated variation of the three theoretical time constants τ for 100-μm CNTs for various values of the axial thermal diffusivity.

XI. ANALYSIS OF THERMAL TIME-SIGNATURE RESULTS

The thermal signatures for CNTs of differing lengths grown on AlN were all fitted to a function of three exponentials, although for the shorter tubes ($L < 60$ μm) a double or single exponential plus a small constant value fitted the data well. The data are consistent with negligible thermal resistance to the substrate. Figure 12 shows the quadratic variation of the dominant time constant as a function of CNT length, which yields an *effective* axial diffusivity of $(8.5 \pm 3) \times 10^{-5}$ m^2 s^{-1}. This effective diffusivity is consistent with the theoretical values found from simulations such as Fig. 11, and assumes that the thermal time constant of the tubes is of the form $\tau = L^2/\kappa$, where L is the tube length. The dominant time constant in each case was determined from the relative amplitudes of the double or triple exponential fits and comparison with the value of a single exponential fit to the data. For short tube lengths $\leqslant 40$ μm, fits for one, two, or three exponentials were consistent, with the two- and

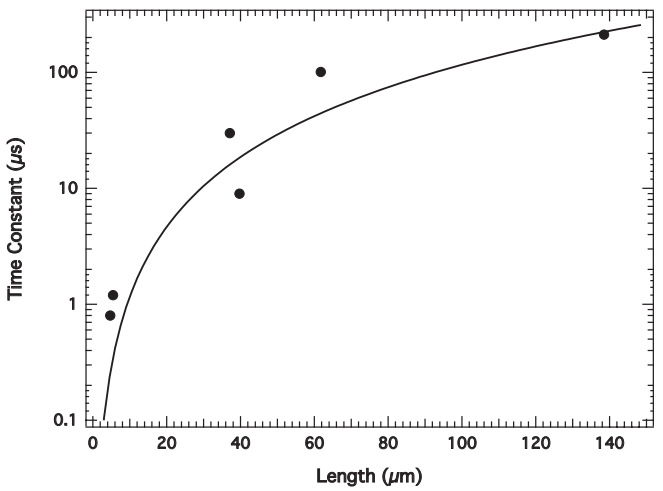

FIG. 12. Quadratic fit to dominant experimental time constant vs. CNT length. It gives a thermal diffusivity of $(8.5 \pm 3) \times 10^{-5}$ m^2 s^{-1}.

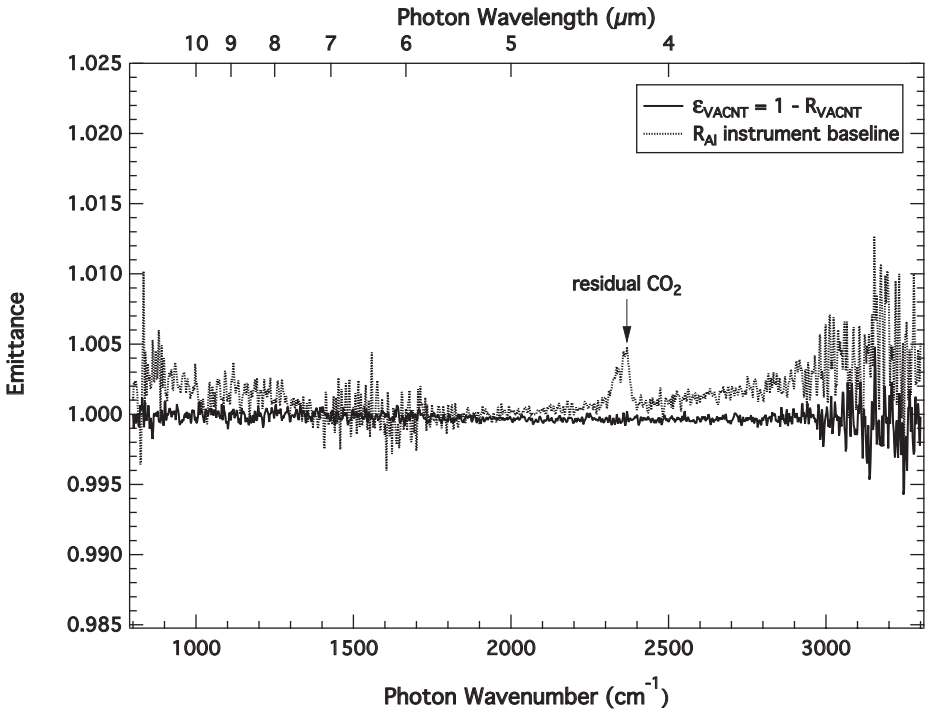

FIG. 13. Near-normal VACNT emittance compared to the instrument baseline.

three-exponential fits giving one dominant contribution that agreed with a single exponential fit. For longer tubes the values obtained from one-, two-, and three-exponential fits to the data for various tube lengths are given in Appendix C. The value of effective axial diffusivity determined in this way is consistent with other reported values of the thermal diffusivity,[13,20] although there is considerable variation of the thermal conductivity reported in the literature, with variations between single- and multi-wall CNTs and between single tubes and bundles (see Ref. 13 and references therein).

XII. CONCLUSIONS

We have characterized the time-dependent thermal emission from pulsed-laser irradiated VACNT arrays and determined their absorptivity, emissivity, and BRDF properties. Laser irradiated VACNTs provide a fast-response source of blackbody radiation. The time dependence of the thermal signal follows a three-exponential decay. For short CNTs, a single-exponential decay is sufficient to represent the thermal signal well. If thermal resistance to substrate is assumed to be negligible, the effective axial diffusivity is about 10^{-4} m^2 s^{-1}.

ACKNOWLEDGMENTS

We would like to thank the staff at the University of Maryland's Nanocenter Fablab and Nanoscale Imaging Spectroscopy and Properties Laboratory for their assistance with characterization of our experimental samples. Funding

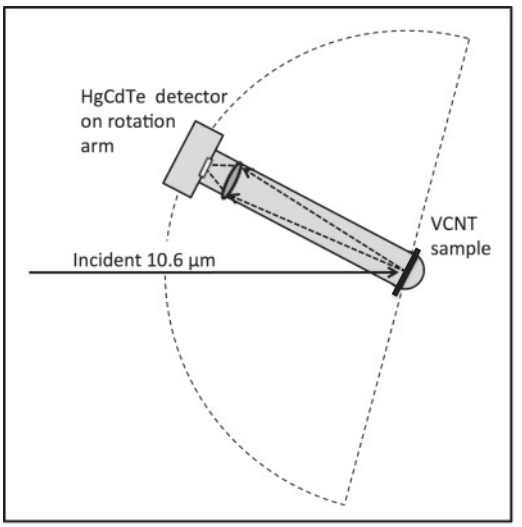

FIG. 14. Schematic of in-plane BRDF measurement (not to scale).

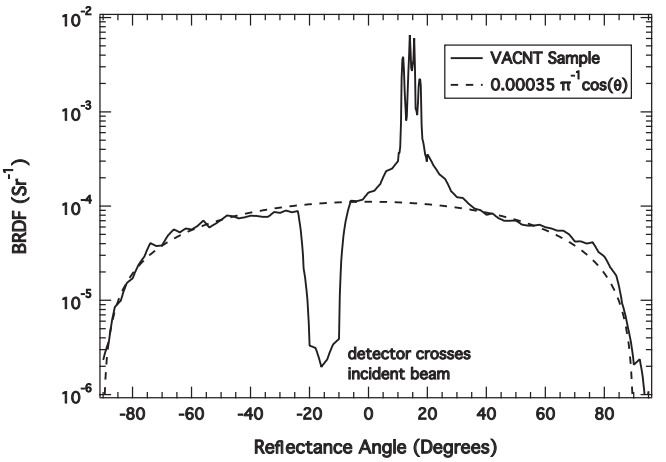

FIG. 15. In-plane BRDF measurement compared to Lambertian reflectance curve.

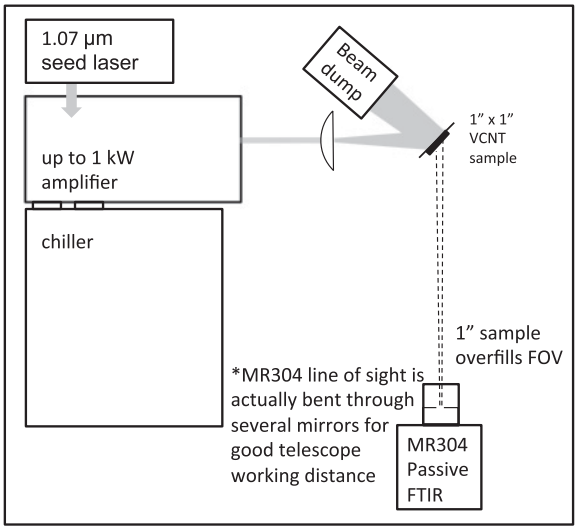

FIG. 16. Emissivity measurement setup.

for this work was made possible by a JHU-APL independent research and development grant.

APPENDIX A: SPECTRAL REFLECTANCE AND BRDF

Room temperature near-normal spectral reflectance of a 30-minute-growth VACNT sample was measured on a Fourier transform infrared (FTIR) spectrometer (Bomem DA3 upgraded to DA8) (full angle acceptance cone of 11°) at 4 cm^{-1} resolution under nitrogen purge, using an aluminum flat mirror as reference and averaging 64 scans per dataset. A measure of instrument baseline stability was obtained as the ratio of mirror reflectance in consecutive datasets. In Fig. 13, measurement results over the range 770 to 3300 cm^{-1} (3 to 13 μm) are presented as near-normal emittance, $\varepsilon = 1-R$, and compared to the instrument baseline stability. Because the instrument baseline should optimally be equal to 1, variance from 1 can be considered an estimate of the measurement limits of the spectrometer. The standard deviation of the baseline from the nominal value of 1 is 0.0025. Values of ε appear to be equal to or less than the baseline deviation; we therefore infer a lower limit of 0.9975 for the near-normal emittance across this spectral range.

Total integrated reflectance (TIR) at a 15° incident angle was measured for a 5-minute-growth VACNT sample at 10.6 μm using a stabilized CO_2 laser. The BRDF was measured with a cooled HgCdTe detector and collection lens fixed to an automated rotation arm, as shown in Fig. 14.

Experimentally, $\mathrm{BRDF}(\theta) = (P/P_{\mathrm{inc}})/(\Omega)$, where P_{inc} is incident laser power, P is the power measured at the given scattering angle, and Ω is the solid angle subtended by the 1-inch-diameter AR-coated ZnSe collection lens at 28 cm from the sample. The BRDF curve, shown in Fig. 15, was integrated (after extrapolating through the dropout due to the detector crossing the incident beam) assuming symmetry in the polar angle according to

$$R_{\mathrm{TOTAL}} = \cos(\theta_{\mathrm{inc}})\pi \int \mathrm{BRDF}(\theta_{\mathrm{scat}}) \sin(\theta_{\mathrm{scat}} + \theta_{\mathrm{inc}}) d\theta \tag{A1}$$

to give $R_{\mathrm{TOTAL}} = 0.0004$, which can be compared to the Lambertian phase function also shown in Fig. 15, for which $R_{\mathrm{TOTAL}} = 0.00035$. At near-normal incident angles, the BRDF is therefore largely Lambertian in form and can be attributed to incoherent scatter. The pronounced specular component is

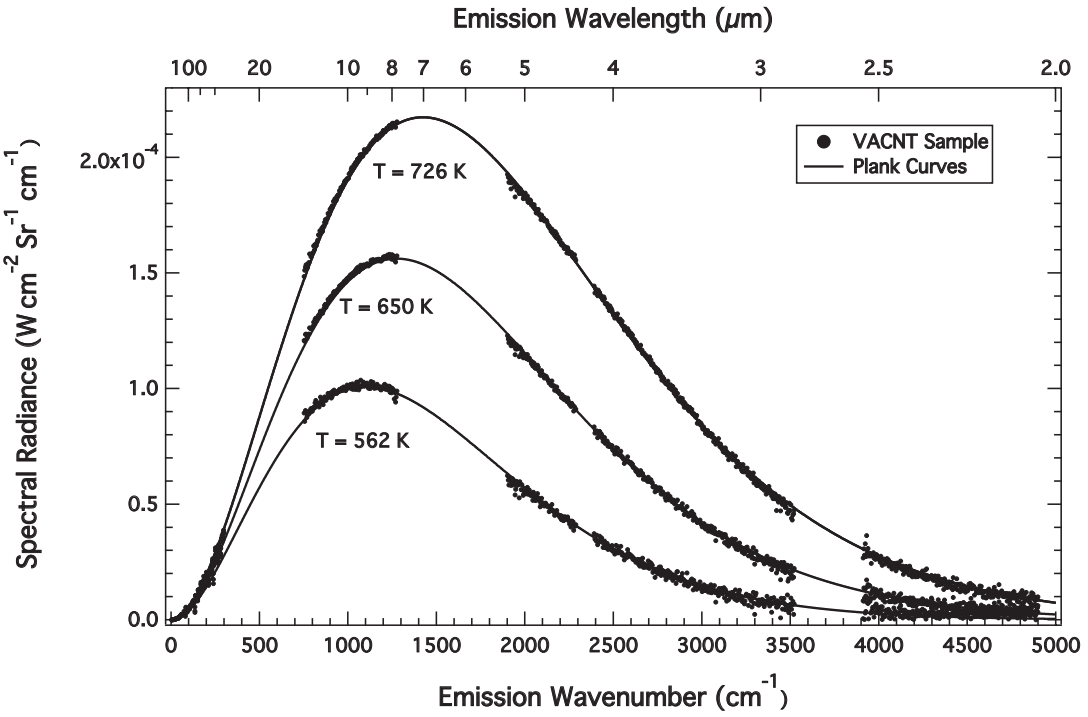

FIG. 17. VACNT spectral emission compared to Planck curves at the measured sample temperature.

well described by a diffuse phase function (partially coherent scatter) with a small admixture of a near-specular phase function (coherent scatter).[21,22] Grating-like effects caused by ordered structure can be seen as sharp spikes near the peak.

APPENDIX B: EMISSIVITY

Emissivity measurements at raised temperatures were made using a near-IR amplified fiber laser at 1.07 μm capable of producing up to 1 kW to heat the sample, while an FTIR spectroradiometer (Bomem MR304) measured emitted radiance over the range 2 to 20 μm, as illustrated in Fig. 16. A calibrated cavity blackbody source with a 1-inch aperture was situated in the sample position, at an optical path distance of 36 feet, safely beyond the 33-foot minimum working distance for the FTIR with its telescope. The line of sight of the instrument was normal to the cavity aperture. The instrument FOV subtended an elliptical region about 0.25 × 0.5 inches, and was centered on the 1-inch blackbody aperture to ensure a filled FOV. The 1-inch-square VACNT sample, fixed to an aluminum plate by silver paint and small clamps at the sample edge, was inserted directly in front of and parallel to the blackbody aperture so that the calibration geometry reproduced the sample test conditions. The blackbody source was removed to permit laser heating of the Al plate at the back of the sample. After testing, the cavity blackbody was replaced to perform calibrations; post-test calibrations were found to be desirable because heating within the closed, interlocked laser room led to small changes in the HgCdTe detector response.

Figure 17 shows calibrated spectral radiance (regions of water and CO_2 absorption have been removed) emitted by the laser-heated VACNT sample, together with least-squares fits of a Planck gray-body radiance function given by

$$L(\nu,T,\varepsilon) = \varepsilon \frac{2hc^2\nu^3}{e^{hc\nu/k_BT} - 1}, \tag{B1}$$

where ν is the emitted light wave number and h, c, and k_B are Planck's constant, the speed of light, and the Boltzmann constant, respectively. In fitting the data, sample temperature T and spectrally constant emissivity coefficient ε were allowed to vary, but in all cases emissivity values of 1 resulted, in good agreement with the BRDF measurement, which gave $\varepsilon = 0.9996$.

APPENDIX C: TIME CONSTANTS FROM MULTIEXPONENTIAL FITS TO OBSERVED TEMPERATURE-TIME SIGNATURES

Table I shows the values for multiexponential fits to experimental temperature versus time signatures for tubes of different lengths. In each case, we use as the dominant time constant the longest time constant obtained from a fit needing the fewest number of exponentials. These are shown in italics in the table.

TABLE I. Results from multiexponential fits of the form $T(t) = \sum A_i e^{-t/\tau_i} + \text{constant}$.

Length (μm)	Three-exp. fit Parameters		Two-exp. fit Parameters		One-exp. fit Parameters	
139	A1	215.851	A1	225.722		No Fit
	τ1	3.51	τ1	7.19		
	A2	79.269	A2	88.019		
	τ2	28.2	τ2	*212*		
	A3	73.948				
	τ3	317				
62	A1	172.495	A1	176.733		No Fit
	τ1	7.8	τ1	8.77		
	A2	183.651	A2	225.26		
	τ2	88.9	τ2	*109*		
	A3	52.85				
	τ3	182				
37	A1	172.406	A1	172.681		No Fit
	τ1	2.39	τ1	2.45		
	A2	208.73	A2	207.68		
	τ2	29.2	τ2	*29.72*		
	A3	4.359				
	τ3	2595				
40	A1	280.963	A1	216.825	A1	353.837
	τ1	4.02	τ1	3.56	τ1	*7.6*
	A2	11.953	A2	78.365		
	τ2	19.1	τ2	6.17		
	A3	3.198				
	τ3	−0.001006436				
5	A1	677.412	A1	629.876	A1	646.459
	τ1	1.24	τ1	1.32	τ1	*1.3*
	A2	3.23	A2	6.242		
	τ2	21	τ2	67.3		
	A3	8.228				
	τ3	0.001266036				
5	A1	637.91	A1	658.687	A1	571.127
	τ1	0.79	τ1	0.786	τ1	*0.87*
	A2	3.68	A2	3.432		
	τ2	45.5	τ2	89.4		
	A3	4.839				
	τ3	5006				

*raul.fainchtein@jhuapl.edu

[1] Z.-P. Yang, L. Ci, J. A. Bur, S.-Y. Lin, and P. M. Ajayan, Nano Lett. **8**, 446 (2008).

[2] H. Bao, X. Ruan, and T. S. Fisher, Opt. Express **18**, 6347 (2010).

[3] K. Mizuno, J. Ishii, H. Kishida, Y. Hayamizu, S. Yasuda, D. N. Futaba, M. Yumura, and K. Hata, Proc. Natl. Acad. Sci. **106**, 6044 (2009).

[4] C. Ni and P. R. Bandaru, Carbon **47**, 2898 (2009).

[5]H. Shi, J. G. Ok, H. W. Baac, and L. J. Guo, Appl. Phys. Lett. **99**, 211103 (2011).
[6]X. J. Wang, J. D. Flicker, B. J. Lee, W. J. Ready, and Z. M. Zhang, Nanotechnol. **20**, 215704 (2009).
[7]X. J. Wang, L. P. Wang, O. S. Adewuyi, B. A. Cola, and Z. M. Zhang, Appl. Phys. Lett. **97**, 163116 (2010).
[8]Z.-P. Yang, M.-L. Hsieh, J. A. Bur, L. Ci, L. M. Hanssen, B. Wilthan, P. M. Ajayan, and S.-Y. Lin, Appl. Opt. **50**, 1850 (2011).
[9]S. Berber, Y.-K. Kwon, and D. Tománek, Phys. Rev. Lett. **84**, 4613 (2000).
[10]D. N. Futaba *et al*., Nature Mater. **5**, 987 (2006).
[11]K. Hata, D. N. Futaba, K. Mizuno, T. Namai, M. Yumura, and S. Iijima, Science **306**, 1362 (2004).
[12]K. Cho and C. C. Davis, IEEE J. Quantum Electron. **25**, 1112 (1989).
[13]M. Akoshima, K. Hata, D. N. Futaba, K. Mizuno, T. Baba, and M. Yumura, Jpn. J. Appl. Phys. **48**, 05EC07 (2009).
[14]W. Yi, L. Lu, Z. Dian-lin, Z. W. Pan, and S. S. Xie, Phys. Rev. B **59**, R9015 (1999).
[15]H. Xie, A. Cai, and X. Wang, Phys. Lett. A **369**, 120 (2007).
[16]V. E. Gusev and A. A. Karabutov, *Laser Optoacoustics* (AIP, New York, 1993).
[17]H. S. Carslaw and J. C. Jaeger, *Conduction of Heat in Solids* (Oxford University Press, London, 1959).
[18]J. V. Beck, K. D. Cole, A. Haji-Sheikh, and B. Litkouhi, *Heat Conduction Using Green's Functions* (Hemisphere, London, 1992).
[19]S. Haque, C. Marinelli, F. Udrea, and W. Milne, in *Technical Proceedings of the 2006 NSTI Nanotechnology Conference and Trade Show*, Vol. 1 (NSTI NanoTech., Boston, MA, 2006), pp. 134–137.
[20]A. Okamoto, I. Gunjishima, T. Inoue, M. Akoshima, H. Miyagawa, T. Nakano, T. Bab, M. Tanemura, and G. Oomi, Carbon **49**, 294 (2011).
[21]M. E. Thomas, *Optical Propagation in Linear Media* (Oxford University Press, New York, 2006).
[22]M. E. Thomas, R. I. Joseph, W. J. Tropf, and A. M. Brown, Proc. SPIE **7792**, 77920I (2010).